nature photonics

LETTERS

https://doi.org/10.1038/s41566-020-00729-z

Check for updates

Optical analogue of Dresselhaus spin–orbit interaction in photonic graphene

C. E. Whittaker[1]✉, T. Dowling[1], A. V. Nalitov[2,3,4], A. V. Yulin[4], B. Royall[1], E. Clarke[5], M. S. Skolnick[1,4], I. A. Shelykh[3,4] and D. N. Krizhanovskii[1,4]✉

The concept of gauge fields plays a significant role in many areas of physics, from particle physics and cosmology to condensed-matter systems, where gauge potentials are a natural consequence of electromagnetic fields acting on charged particles and are of central importance in topological states of matter[1]. Here, we report on the experimental realization of a synthetic non-Abelian gauge field for photons[2] in a honeycomb microcavity lattice[3]. We show that the effective magnetic field associated with transverse electric–transverse magnetic splitting has the symmetry of the Dresselhaus spin–orbit interaction around Dirac points in the dispersion, and can be regarded as an SU(2) gauge field[4]. The symmetry of the field is revealed in the optical spin Hall effect, where, under resonant excitation of the Dirac points, precession of the photon pseudospin around the field direction leads to the formation of two spin domains. Furthermore, we observe that the Dresselhaus-type field changes its sign in the same Dirac valley on switching from *s* to *p* bands, in good agreement with the tight-binding modelling. Our work demonstrating a non-Abelian gauge field for light on the microscale paves the way towards manipulation of photons via spin on a chip.

Gauge fields are central to the description of fundamental forces and can carry profound physical consequences. In the case of electromagnetism, for example, the significance of the magnetic vector potential **A** is revealed by a quantum-mechanical phase shift experienced by charged particles in the celebrated Aharonov–Bohm (AB) effect. Although this is a manifestation of a U(1) Abelian gauge field with scalar components, there also exist spin-dependent vector potentials with non-commuting components (first considered by Yang and Mills), that is, SU(2) non-Abelian gauge fields[5]. In condensed-matter physics, the non-Abelian framework is also highly relevant[6], in particular to the theory of spin–orbit coupling (SOC) in solids[7,8], which plays an indispensable role in the family of spin Hall effects[9], topological insulators and superconductors[1], as well as the operation of spintronic devices[10]. On the other hand, photons—neutral particles with zero magnetic moment—can also behave as if affected by both Abelian and non-Abelian gauge fields in suitably designed environments[11]. These allow the exploration of gauge field Hamiltonians in the optical domain, and a means of manipulating light trajectories and internal degrees of freedom such as spin (polarization) for spinoptronic signal processing applications[12]. Abelian gauge fields have been engineered in diverse platforms including silica waveguides[13], metamaterials[14], silicon ring resonators[15,16] and liquid-crystal optical cavities[17]. By contrast, the realization of non-Abelian gauge fields in photonic microstructures and thus enabling manipulation of light via spin on a chip remains a significant challenge.

One possible way to implement artificial non-Abelian gauge fields on the microscale in a monolithic structure is to use the reduced spatial symmetry of birefringent[18,19] or laterally patterned[4,20] semiconductor microcavities along with native transverse electric–transverse magnetic (TE–TM) splitting (photonic SOC). Honeycomb lattices are of particular interest, because they provide access to the physics of graphene and related materials, including the Dirac dispersion[3], edge states[21] and influence of strain[22], all in a controlled photonic environment in which some of the limitations of real graphene can be overcome. Importantly, although graphene itself suffers from small SOC, which prevents observation of the spin Hall effect, the photonic SOC can be enhanced in wavelength-scale photonic lattices[23,24], enabling the physics of non-Abelian gauge fields in graphene geometries to be explored.

In this Letter, we utilize a patterned GaAs-based microcavity with a honeycomb lattice geometry (Fig. 1a)—that is, photonic graphene—to study the influence of photonic SOC on the dispersion. In this setting (see Methods for sample details), which was previously considered theoretically in ref. [4], the interplay between the SOC and the reduced spatial symmetry imposed by the lattice transforms the double winding effective magnetic field associated with TE–TM splitting into a Dresselhaus-type field with a single winding locally around the Dirac points, which can be described in terms of a non-Abelian gauge field. Here, we visualize the field texture around these high symmetry points, and further confirm the Dresselhaus symmetry by the optical spin Hall effect (OSHE) revealing the formation of two cross-polarized spin domains. Our results are in good agreement with the theory presented in ref. [4] and demonstrate the potential for engineering artificial gauge fields for photons in different orbital bands using model two-dimensional (2D) lattice systems. Finally, we note that the non-Abelian AB effect has been observed recently by cascading non-reciprocal optical elements in a fibre-optic set-up (that is, not on the microscale and governed by physical mechanisms that are very different from those reported in the present manuscript)[25].

To measure the dispersion relation of our sample we use low-power incoherent excitation to populate all modes. The band structure features linear Dirac crossings at characteristic momenta, namely the K and K′ points at the Brillouin zone (BZ) corners (Fig. 1b), which are visible in the angle-resolved photoluminescence (PL) spectra shown for the fundamental *s* bands and higher-energy *p* bands plotted along high-symmetry directions in Fig. 1c,d (different slices of momentum space are selected for maximal

[1]Department of Physics and Astronomy, University of Sheffield, Sheffield, UK. [2]Faculty of Science and Engineering, University of Wolverhampton, Wolverhampton, UK. [3]Science Institute, University of Iceland, Reykjavik, Iceland. [4]ITMO University, St Petersburg, Russia. [5]EPSRC National Epitaxy Facility, University of Sheffield, Sheffield, UK. ✉e-mail: charles.whittaker@sheffield.ac.uk; d.krizhanovskii@sheffield.ac.uk

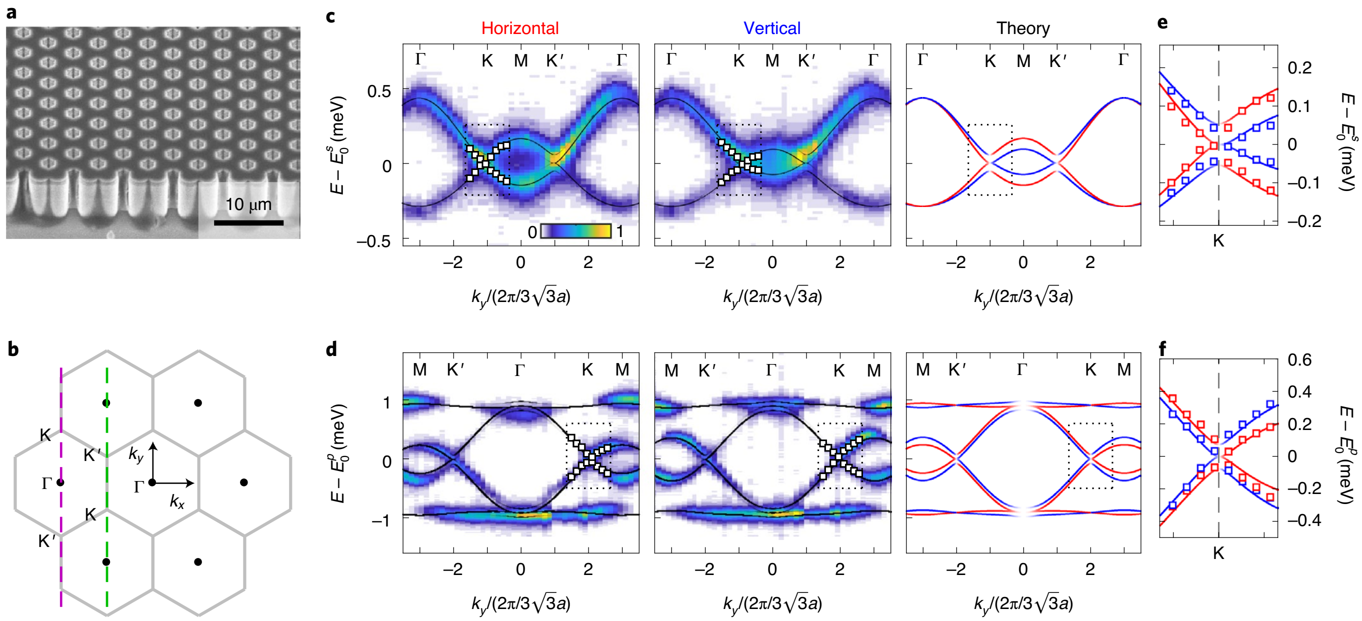

Fig. 1 | Photonic graphene sample and dispersion relations. a, Scanning electron microscope image of the honeycomb lattice. **b**, Schematic of the reciprocal space lattice. **c**, Polarization-resolved PL spectra showing *s* bands along the dashed green line in **b** with tight-binding (TB) calculations (solid curves). Left: horizontal polarization (H). Middle: vertical polarization (V). The white squares inside the dotted rectangles show the peak positions extracted from the experimental data. Right: corresponding polarization-resolved dispersion relation calculated by the TB model. E_0^s is 1.4551 eV. **e**, Zoom-in on the dotted rectangles in **c**. The red and blue squares (lines) show the experimental (theoretical) horizontal and vertical dispersions, respectively. **d**,**f**, Same as in **c** and **e** but for the *p* bands, shown along the purple dashed line in **b**. E_0^p is 1.4582 eV. *a* is the lattice constant.

signal intensity; Supplementary Section 5). By resolving the emission in linear polarization, the orientation of the TE–TM splitting effective magnetic field at each energy and momentum can be revealed, because it corresponds to the pseudospin of the eigenstate. Hence, to characterize the pseudospin texture and therefore the field orientation across momentum space, we measure the first two Stokes parameters S_1 and S_2 of the emission (Methods). For both *s* and *p* bands, a pronounced splitting between TE and TM modes (which have horizontal (H) and vertical (V) polarization for the directions plotted) is visible, which is well described using a TB formalism including SOC as in refs. [4,26] (Methods). Importantly, the pseudospin changes sign as the *k* vector passes through a Dirac point, as we show using a zoom on the K point. This suggests that, locally, around a K or K′ point the dependence of TE–TM splitting on momentum differs from that found in a planar cavity around $\mathbf{k} = 0$. To study this polarization behaviour in more detail, we constructed 2D energy-resolved polarization maps using tomographic imaging (Methods).

First we will focus on the *s* bands. In Fig. 2, we see 2D maps of the linear polarization angle ϕ in momentum space, calculated as $2\phi = \arctan(S_2/S_1)$. For the Γ point, which corresponds to the emission around $\mathbf{k} = 0$ at the energy minimum of the dispersion, a quadrupole pattern can be seen (Fig. 2a). Arrows showing the pseudospin texture (orientation of the effective magnetic field) reveal the familiar dipolar field associated with TE–TM splitting in microcavities. Figure 2c,e shows the corresponding maps at the energy of the Dirac points. In contrast to the Γ point, the local symmetry around K and K′ no longer has a double azimuthal dependence. Rather, there is a single winding of the pseudospin with the characteristic texture of a Dresselhaus-type field[27]. We note that the local effective magnetic fields have opposite sign around the K and K′ points, although the direction of field rotation is the same (counter-rotating with the azimuthal angle). These features can also be seen clearly in calculations using the TB model of ref. [4] (Fig. 2b,d,f), where there is excellent agreement with the experiment. As we show in the Methods, using a suitable minimal coupling transformation the observed effective field around the Dirac points can be described in terms of a non-Abelian gauge field with non-commuting components. By contrast, around the Γ point, the SOC has the same form as for unpatterned microcavities and cannot be described in terms of a synthetic gauge field.

One of the clearest manifestations of the effective magnetic field acting on photons is the formation of spin currents in the OSHE, caused by pseudospin precession around the *k*-dependent effective magnetic field[28]. At a given energy, the wavevector and polarization of the injected light can be used to control the spin texture of the emission, because the pseudospin rotation depends on the relative angle between its initial direction and the effective field. We use this knowledge to unveil the different symmetries shown in Fig. 2 by imaging the time-integrated real space emission of our sample under continuous optical excitation at the Γ, K and K′ points with a linearly polarized pump. We vary the energy and angle of the incoming laser to excite these points in the dispersion and measure the resulting emission intensity in right and left circular polarizations to determine the Stokes parameter S_3 (Methods). In Fig. 3a we show how resonant excitation at the Γ point under H-polarized excitation indeed leads to the observation of four domains with alternating circular polarization, confirming that at the energy minimum of the dispersion, at the centre of the BZ, the effective magnetic field in Fig. 2a has the same form as that of conventional planar microcavities[4,29]. In contrast, under H-polarized pumping at the K point (Fig. 3c), only two domains are seen, formed to the left and right of the pump spot and with opposite circular polarizations as expected from the Dresselhaus symmetry surrounding the Dirac points (Fig. 2c,e). This is expected, because the injected pseudospin vector lies parallel/anti-parallel to the field direction along the k_y axis in the locally excited region of momentum space, so there should be no evolution of the pseudospin along *y*.

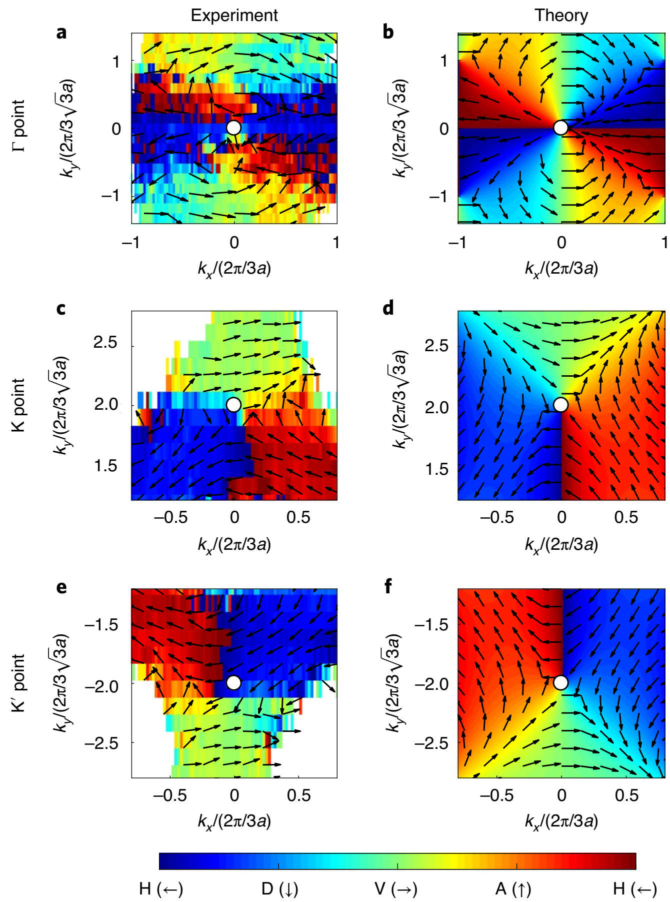

Fig. 2 | Texture of the effective magnetic fields surrounding Γ, K and K′ points. **a**,**c**,**e**, Experimental momentum space maps of ϕ at the energy of the Γ point (1.4547 eV) and K and K′ points (1.4551 eV), respectively, with arrows representing the pseudospin vector. White regions correspond to low signal intensity (<5% of maximum). **b**,**d**,**f**, Corresponding calculated momentum space maps of ϕ at the energy of the Γ, K and K′ points, respectively, with arrows representing the pseudospin vector. D and A denote diagonal and anti-diagonal polarizations, respectively. Note that the lowest and highest values on the colour scale correspond to the same polarization.

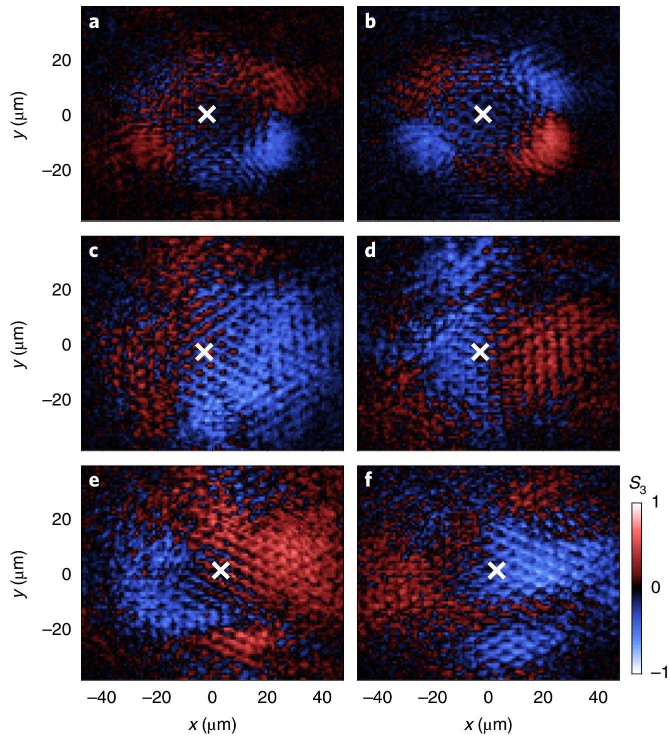

Fig. 3 | Observation of the OSHE. **a**,**c**,**e**, Measured real-space circular polarization degree S_3 under resonant excitation at the Γ (**a**), K (**c**) and K′ (**e**) points with H-polarized pump. **b**,**d**,**f**, Corresponding results for a V-polarized pump. The energies used for excitation of the Γ and K/K′ points are 1.4547 eV and 1.4551 eV, respectively. The cross in each panel marks the position of the pump spot.

When the excitation angle is changed to excite the K′ point instead (Fig. 3e), the pattern is reversed, as expected, because the sign of the Dresselhaus-type field is opposite. Our results are in strong qualitative agreement with theoretical spin patterns calculated using the gauge-field Hamiltonian (Supplementary Section 1) as well as the numerical simulations of ref. [4]. In Fig. 3b,d,f we demonstrate that, upon changing to V-polarized excitation, the patterns shown in Fig. 3a,c,e are all reversed because the initial pseudospin vector points in the opposite direction[28], which confirms that the observed spin patterns result from precession of the pseudospin vector in the OSHE regime.

Now we turn our attention to the p bands. Using the same procedure as that of Fig. 2, we determine the texture of the effective magnetic field across momentum space at the energy of the Dirac points to reveal the local symmetry surrounding the K and K′ points. The full momentum space linear polarization map (Supplementary Section 5) confirms that the local symmetry around these points has the form of Dresselhaus SOC (with opposite sign for K and K′), as is the case for the s bands. We show the field surrounding a K point in Fig. 4a, where a clear single winding of the Dresselhaus type is visible. Note that the sign of the field for a given valley (K or K′) is opposite to the case of the s bands (as seen also in Fig. 1). Our finding is supported by the TB model developed for the p orbitals[26], where the calculated field texture shows excellent agreement (Fig. 4b). To further confirm the Dresselhaus-type fields, we performed OSHE measurements by coherently exciting the p bands. In Fig. 4c–f we show results for resonant excitation of the K and K′ points at $k_y/(2\pi/3\sqrt{3}a) = \pm 2$ (Fig. 4c,e respectively). Clear two-fold circular polarization patterns can be seen, which rotate when the excitation polarization is changed from H to V (Fig. 4d,f). These findings are in good agreement with theoretical calculations (Supplementary Section 1).

In summary, we have experimentally demonstrated the existence of local Dresselhaus-type fields surrounding the Dirac points in photonic graphene, confirmed by the generation of two-fold circular polarization patterns in the OSHE. Our findings constitute the realization of a synthetic SU(2) non-Abelian gauge field induced by the presence of the honeycomb periodic potential, which leads to a TE–TM effective magnetic field with a modified texture at specific points in momentum space. We note that although such fields may be engineered in other lattices featuring Dirac cones, such as Kagome lattices[30], it is not possible in other geometries such as Lieb lattices due to the square symmetry. Practically speaking, our findings offer a means of separating and routing spins, where the single-winding effective magnetic field (odd in k) analogous to electronic systems is highly advantageous because it leads to counter-propagation of opposite spins. Further fundamental consequences of the non-Abelian gauge field on the motion of wavepackets may be studied using the zitterbewegung effect (Supplementary Section 3). This field is also responsible for the emergence of topologically nontrivial

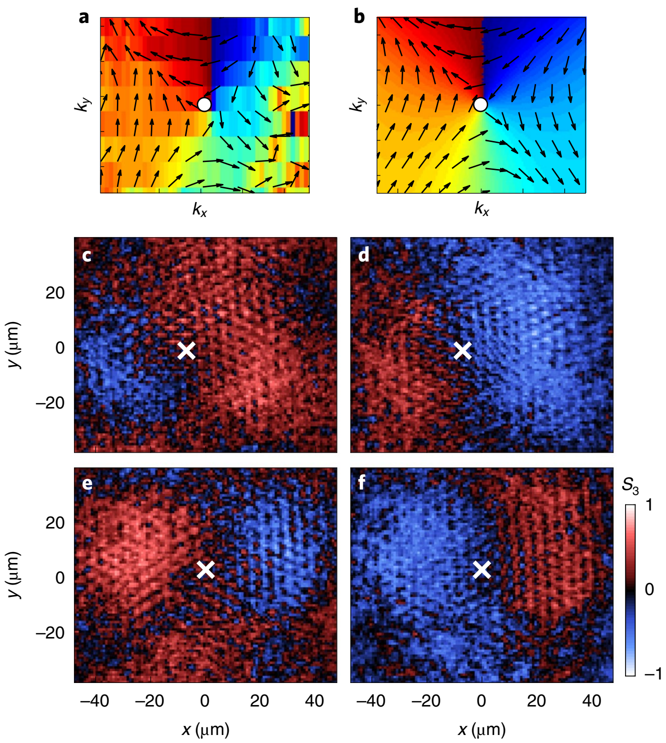

Fig. 4 | Effective magnetic field texture and OSHE for *p* bands. **a**, Experimentally obtained effective magnetic field texture surrounding a K point. **b**, Corresponding calculated effective magnetic field texture surrounding a K point. **c**,**e**, Measured real-space circular polarization degree S_3 under resonant excitation at the K (**c**) and K′ (**e**) points with an H-polarized pump. **d**,**f**, Corresponding results for a V-polarized pump. The energy used for excitation is 1.4582 eV. The crosses in **c**–**f** mark the position of the pump spot.

gaps in the polariton spectrum in the presence of external magnetic fields breaking time-reversal symmetry (which is not broken in our system)[31,32]. In microcavities with a small exciton–photon detuning, the addition of spin-anisotropic polariton–polariton interactions to the present system opens up new possibilities, including spin-dependent Klein tunnelling[20], interaction-induced topological phase transitions[33] and potentially a nonlinear modification of the spin domains[34]. We also anticipate that, in principle, the gauge field realized in our system may be engineered in other platforms such as photonic crystals based on thick slab waveguides with small TE–TM splitting[35] or plasmonic lattices[36]. The study of the non-Abelian gauge fields acting on photon spin in topological lattices with special symmetries would also be an interesting research direction[37].

Online content

Any methods, additional references, Nature Research reporting summaries, source data, extended data, supplementary information, acknowledgements, peer review information; details of author contributions and competing interests; and statements of data and code availability are available at https://doi.org/10.1038/s41566-020-00729-z.

Received: 26 February 2020; Accepted: 20 October 2020;
Published online: 30 November 2020

References

1. Qi, X.-L. & Zhang, S.-C. Topological insulators and superconductors. *Rev. Mod. Phys.* **83**, 1057–1110 (2011).
2. Chen, Y. et al. Non-Abelian gauge field optics. *Nat. Commun.* **10**, 3125 (2019).
3. Jacqmin, T. et al. Direct observation of Dirac cones and a flatband in a honeycomb lattice for polaritons. *Phys. Rev. Lett.* **112**, 116402 (2014).
4. Nalitov, A. V., Malpuech, G., Terças, H. & Solnyshkov, D. D. Spin–orbit coupling and the optical spin Hall effect in photonic graphene. *Phys. Rev. Lett.* **114**, 026803 (2015).
5. Yang, C. N. & Mills, R. L. Conservation of isotopic spin and isotopic gauge invariance. *Phys. Rev.* **96**, 191–195 (1954).
6. Wilczek, F. & Zee, A. Appearance of gauge structure in simple dynamical systems. *Phys. Rev. Lett.* **52**, 2111–2114 (1984).
7. Fröhlich, J. & Studer, U. M. Gauge invariance and current algebra in nonrelativistic many-body theory. *Rev. Mod. Phys.* **65**, 733–802 (1993).
8. Jin, P.-Q., Li, Y.-Q. & Zhang, F.-C. SU(2) × U(1) unified theory for charge, orbit and spin currents. *J. Phys. A* **39**, 7115–7123 (2006).
9. Sinova, J., Valenzuela, S. O., Wunderlich, J., Back, C. H. & Jungwirth, T. Spin Hall effects. *Rev. Mod. Phys.* **87**, 1213–1260 (2015).
10. Ohno, H., Stiles, M. D. & Dieny, B. Spintronics. *Proc. IEEE. Inst. Electr. Electron. Eng.* **104**, 1782–1786 (2016).
11. Aidelsburger, M., Nascimbene, S. & Goldman, N. Artificial gauge fields in materials and engineered systems. *Comptes Rendus Phys.* **19**, 394–432 (2018).
12. Shelykh, I. A., Kavokin, A. V. & Malpuech, G. in *Spin Dynamics of Exciton Polaritons in Microcavities* Ch. 9, 187–210 (Wiley, 2007).
13. Rechtsman, M. C. et al. Strain-induced pseudomagnetic field and photonic Landau levels in dielectric structures. *Nat. Photon.* **7**, 153–158 (2013).
14. Liu, F., Xu, T., Wang, S., Hang, Z. H. & Li, J. Polarization beam splitting with gauge field metamaterials. *Adv. Opt. Mater.* **7**, 1801582 (2019).
15. Hafezi, M., Mittal, S., Fan, J., Migdall, A. & Taylor, J. M. Imaging topological edge states in silicon photonics. *Nat. Photon.* **7**, 1001–1005 (2013).
16. Mittal, S. et al. Topologically robust transport of photons in a synthetic gauge field. *Phys. Rev. Lett.* **113**, 087403 (2014).
17. Rechcińska, K. et al. Engineering spin–orbit synthetic Hamiltonians in liquid–crystal optical cavities. *Science* **366**, 727–730 (2019).
18. Gianfrate, A. et al. Measurement of the quantum geometric tensor and of the anomalous Hall drift. *Nature* **578**, 381–385 (2020).
19. Fieramosca, A. et al. Chromodynamics of photons in an artificial non-Abelian magnetic Yang–Mills field. Preprint at https://arxiv.org/abs/1912.09684 (2019).
20. Solnyshkov, D., Nalitov, A., Teklu, B., Franck, L. & Malpuech, G. Spin-dependent Klein tunneling in polariton graphene with photonic spin–orbit interaction. *Phys. Rev. B* **93**, 085404 (2016).
21. Milićević, M. et al. Edge states in polariton honeycomb lattices. *2D Mater.* **2**, 034012 (2015).
22. Milićević, M. et al. Type-III and tilted Dirac cones emerging from flat bands in photonic orbital graphene. *Phys. Rev. X* **9**, 031010 (2019).
23. Sala, V. G. et al. Spin–orbit coupling for photons and polaritons in microstructures. *Phys. Rev. X* **5**, 011034 (2015).
24. Whittaker, C. E. et al. Exciton polaritons in a two-dimensional Lieb lattice with spin–orbit coupling. *Phys. Rev. Lett.* **120**, 097401 (2018).
25. Yang, Y. et al. Synthesis and observation of non-Abelian gauge fields in real space. *Science* **365**, 1021–1025 (2019).
26. Zhang, C., Wang, Y. & Zhang, W. Topological phase transition with *p* orbitals in the exciton–polariton honeycomb lattice. *J. Phys. Condens. Matter* **31**, 335403 (2019).
27. Dresselhaus, G. Spin–orbit coupling effects in zinc blende structures. *Phys. Rev.* **100**, 580–586 (1955).
28. Kavokin, A., Malpuech, G. & Glazov, M. Optical spin Hall effect. *Phys. Rev. Lett.* **95**, 136601 (2005).
29. Leyder, C. et al. Observation of the optical spin Hall effect. *Nat. Phys.* **3**, 628–631 (2007).
30. Gulevich, D. R., Yudin, D., Iorsh, I. V. & Shelykh, I. A. Kagome lattice from an exciton–polariton perspective. *Phys. Rev. B* **94**, 115437 (2016).
31. Nalitov, A. V., Solnyshkov, D. D. & Malpuech, G. Polariton $\mathbb{Z}$ topological insulator. *Phys. Rev. Lett.* **114**, 116401 (2015).
32. Klembt, S. et al. Exciton–polariton topological insulator. *Nature* **562**, 552–556 (2018).
33. Bleu, O., Solnyshkov, D. D. & Malpuech, G. Interacting quantum fluid in a polariton Chern insulator. *Phys. Rev. B* **93**, 085438 (2016).
34. Flayac, H., Solnyshkov, D. D., Shelykh, I. A. & Malpuech, G. Transmutation of skyrmions to half-solitons driven by the nonlinear optical spin Hall effect. *Phys. Rev. Lett.* **110**, 016404 (2013).
35. Shapochkin, P. Y. et al. Polarization-resolved strong light-matter coupling in planar GaAs/AlGaAs waveguides. *Opt. Lett.* **43**, 4526–4529 (2018).
36. Bliokh, K. Y., Rodríguez-Fortuño, F. J., Nori, F. & Zayats, A. V. Spin–orbit interactions of light. *Nat. Photon.* **9**, 796–808 (2015).
37. Khanikaev, A. B. & Shvets, G. Two-dimensional topological photonics. *Nat. Photon.* **11**, 763–773 (2017).

Methods

Sample description. Our sample is a GaAs microcavity with 23 (26) top (bottom) GaAs/$Al_{0.85}Ga_{0.15}As$ distributed Bragg reflector pairs and six $In_{0.04}Ga_{0.96}As$ quantum wells, as previously described in ref. [38]. The sample was processed using electron-beam lithography and plasma dry etching to pattern arrays of micropillars with 3-μm diameters and an etch depth on the order of 8 μm. We studied a honeycomb lattice with a pillar-to-pillar separation of 2.8 μm and dimensions of ~120 × 100 μm². The cavity–exciton detuning was approximately −23 meV. The Q factor of the structure was determined to be ~16,000 from the linewidth of 0.09 meV. The size of the TE–TM splitting was ~0.12 meV at $k = 1\,\mu\text{m}^{-1}$.

Excitation scheme. To characterize the dispersion relation of the honeycomb lattice, a low-power non-resonant diode laser was used in reflection geometry to incoherently populate all of the lattice modes. To study the formation of pseudospin domains, we excited the lattice in transmission geometry with a continuous-wave Ti:sapphire laser tuned to be resonant with the honeycomb lattice dispersion. Different states can be excited by varying the energy and angle of incidence θ of the Gaussian laser beam, the latter of which is changed using a translation stage to move the lateral position of the beam before the excitation objective. This allowed us to accurately control the in-plane wavevector of the injected wavepacket because $k = \left(\frac{\omega}{c}\right)\sin\theta$, where ω is the laser frequency. The linear polarization of the injected wavepacket can also be controlled through the use of a linear polarizer and half wave plate in the excitation path. The excitation beam has a full-width at half-maximum of ~15 μm.

Detection scheme. To characterize the pseudospin texture around the Γ, K and K′ points, we measured the polariton PL emission under non-resonant excitation (in the low-density regime far below the condensation threshold) by employing a half wave plate and linear polarizer in the detection path to measure the first two Stokes parameters. These are given by $S_1 = (I_H - I_V)/(I_H + I_V)$ and $S_2 = (I_D - I_A)/(I_D + I_A)$, where I_H, I_V, I_D and I_A give the intensity of emitted light in the horizontal, vertical, diagonal and anti-diagonal polarizations, respectively. By scanning the final lens across the spectrometer slit, multiple E versus k slices were recorded (corresponding to different wavevectors in the direction orthogonal to the spectrometer slit), allowing 2D energy-resolved polarization maps to be constructed. Each map shows a small spectral window of ~20 μeV around the energy of the Γ or Dirac points. Because polariton modes have finite linewidth, there is non-zero PL intensity at k vectors away from these points (for example, $|k - K| > 0$). This PL emission arises from the tail of polariton modes with maxima at energies tens or hundreds of μeV above (or below) the specific energy of interest due to polariton dispersion. The lower intensity of the tails leads to decreased signal-to-noise ratio for further away k vectors, as seen in Figs. 2 and 4.

For the resonant transmission measurements the half wave plate was replaced by a quarter wave plate to measure the third Stokes parameter, which is given by $S_3 = (I_{\sigma^+} - I_{\sigma^-})/(I_{\sigma^+} + I_{\sigma^-})$, where I_{σ^+} and I_{σ^-} correspond to the emission intensity in the right and left circular polarizations, respectively.

Gauge field representation. The pseudospin patterns in Fig. 2 correspond to the eigenstates of the polariton graphene effective Hamiltonian, which has the following form in the vicinity of the Dirac points[4]:

$$H^{\mathrm{D}}(\mathbf{q}) = \hbar v_{\mathrm{F}}\left(\tau_z q_x \sigma_x + q_y \sigma_y\right) + \Delta\left(\tau_z \sigma_y \otimes s_y - \sigma_x \otimes s_x\right) \quad (1)$$

where $\mathbf{q}$ is the wavevector deviation from the corresponding Dirac point set by the valley index $\tau_z = \pm 1$, v_F is the effective Fermi velocity, σ and s are the sublattice and polarization pseudospin operators, and Δ is the effective photonic SOC strength[23]. Prefactors of both terms in Hamiltonian (1) may be expressed in the TB model parameters: $\hbar v_F = 3Ja/2$, $\Delta = 3\delta J/2$ (see next section in Methods for additional details). The spin–orbit term may be included in the low-energy graphene Hamiltonian, represented by the first term in equation (1), with minimal coupling transformation $\mathbf{q} \to \mathbf{q} - \mathbf{A}$ with the gauge field components given by

$$A_x = -\frac{\Delta}{\hbar v_{\mathrm{F}}}\tau_z s_x,\ A_y = \frac{\Delta}{\hbar v_{\mathrm{F}}}\tau_z s_y \quad (2)$$

The artificial gauge field (2) is non-Abelian because the components do not commute[20]. This field is responsible for the suppression of Klein tunnelling[20] and emergence of topologically nontrivial bandgaps of the polariton spectrum in the presence of external magnetic fields[31,32]. Polarization spectral splitting may be also attributed to the effective magnetic field, acting on polariton pseudospin. In the range of energies $\Delta \ll |E| \ll \hbar v_F/a$ this effective SOC is given by the Hamiltonian term $H^{\mathrm{D}}_{\mathrm{SOC}}(\mathbf{q}) = \pm\Delta\left(q_x s_x - q_y s_y\right)/q$, sharing the same angular dependence with the Dresselhaus spin–orbit term in electron systems[27], but constant in the wavevector absolute value q. Note that the sign of the splitting inverts with both valley index τ_z and the sign corresponding to upper and lower Dirac cones.

The Hamiltonian (1) close to Dirac points thus drastically differs from its counterpart in the vicinity of the Γ point

$$H^{\Gamma}(\mathbf{k}) = \hbar^2 k^2/(2m) + \beta\left[s_x(k_x^2 - k_y^2) + 2 s_y k_x k_y\right] \quad (3)$$

where the first term corresponds to a free particle with effective mass $m = \hbar^2/(3Ja^2)$ and the second term describes the action of TE–TM splitting, corresponding to the effective magnetic field with components $\Omega_x = \beta a^2(k_x^2 - k_y^2)$ and $\Omega_y = 2\beta k_x k_y$ with $\beta = 3\delta Ja^2/8$, related to the TB model parameters (see next section in Methods for details). Note that the quadratic dependence of the effective magnetic field on the components of $\mathbf{k}$, fully similar to those reported for the case of an unpatterned cavity, precludes its description in terms of the minimal coupling to a synthetic gauge field and leads to the difference of the effective masses of the longitudinal and transverse polariton modes, $m_{l,t} = m(1 \pm 2m\beta/\hbar^2)$[39].

Effective field derivation near the Dirac point. The effective magnetic field acting on the polariton pseudospin near the Dirac point is obtained by development of the TB Hamiltonian[4]:

$$H_{\mathbf{k}} = -J\sigma_+ - \delta J\sigma_+ \otimes \left(f^+_{\mathbf{k}} s_+ + f^-_{\mathbf{k}} s_-\right) + \mathrm{h.c.} \quad (4)$$

Although the local gauge fields in the vicinities of Dirac points K and K′ were studied in ref. [4], the effective field given by formula (3) near the Γ point, reproducing the symmetry and quadratic k dependence of the TE–TM field in planar microcavities, is also inherent to Hamiltonian (4). In the latter case, the splitting is due to the second-order terms in the complex coefficients:

$$f_{\mathbf{k}} = 3\left(1 - \frac{k^2 a^2}{4}\right),\ f^{\pm}_{\mathbf{k}} = -\frac{3i}{2}k_{\pm}a - \frac{3}{8}k_{\pm}^2 a^2 \quad (5)$$

where $k_\pm = k_x \pm ik_y$. The energy dispersion near the ground state in the corresponding order then reads

$$E^{\pm}_k = -3J\left[1 - \frac{k^2 a^2}{8}\left(1 - \frac{\delta J^2}{J^2} \pm \frac{\delta J}{J}\right)\right] \quad (6)$$

and the Hamiltonian has the form of interaction with the effective TE–TM field (3) of strength given by $\beta = 3\delta Ja^2/8$.

TB parameters used to fit experimental data. To fit the experimental dispersion relations in Fig. 1, for the s bands we use $J = 0.12$ meV and $\delta J = 0.018$ meV. To account for a small asymmetry of the dispersion about the Dirac energy (visible at the Γ point), we add a next-nearest-neighbour correction of −0.008 meV (ref. [3]). For the p bands we used the TB model of ref. [26] with $J = -0.6$ meV and $\delta J = 0.05$ meV, which describes tunnelling of p orbitals with lobes oriented along the link connecting micropillars. In our notation J and δJ corresponds to t and Δt in ref. [26].

Data availability

The data that support the findings of this study are openly available from the University of Sheffield repository at https://doi.org/10.15131/shef.data.13060610.

References

38. Whittaker, C. E. et al. Effect of photonic spin–orbit coupling on the topological edge modes of a Su–Schrieffer–Heeger chain. *Phys. Rev. B* **99**, 081402 (2019).
39. Shelykh, I. A., Nalitov, A. V. & Iorsh, I. V. Optical analog of Rashba spin–orbit interaction in asymmetric polariton waveguides. *Phys. Rev. B* **98**, 155428 (2018).

Acknowledgements

The work was supported by UK EPSRC grants nos. EP/N031776/1 and EP/R04385X/1 and by the Russian Science Foundation (project no. 19-72-20120). I.A.S. acknowledges support from the Icelandic Science Foundation, project 'Hybrid Polaritonics'. A.V.N. acknowledges support from the European Union's Horizon 2020 research and innovation programme under the Marie Skłodowska-Curie grant agreement no. 846353.

Author contributions

C.E.W. and T.D. performed the experiments and analysed the data. E.C. grew the sample. B.R. performed post-growth fabrication. A.V.N. and I.A.S. provided theoretical input. C.E.W., A.V.N. and A.V.Y. performed theory calculations. C.E.W. and D.N.K. designed the experiment. C.E.W., A.V.N., I.A.S., M.S.S. and D.N.K. wrote the manuscript.

Competing interests

The authors declare no competing interests.

Additional information

Supplementary information is available for this paper at https://doi.org/10.1038/s41566-020-00729-z.

Correspondence and requests for materials should be addressed to C.E.W. or D.N.K.

Peer review information *Nature Photonics* thanks Yi Yang and the other, anonymous, reviewer(s) for their contribution to the peer review of this work.

Reprints and permissions information is available at www.nature.com/reprints.